*materials*

MDPI

*Article*

# Synthesis of $Sb_2S_3$ NRs@rGO Composite as High-Performance Anode Material for Sodium-Ion Batteries

**Hosung Hwang [1], Honggyu Seong [1], So Yi Lee [1], Joon Ha Moon [1], Sung Kuk Kim [1], Jin Bae Lee [2], Yoon Myung [3], Chan Woong Na [3,*] and Jaewon Choi [1,*]**

1 Department of Chemistry and Research Institute of Natural Science, Gyeongsang National University, Jinju 52828, Korea; hshwang3@gnu.ac.kr (H.H.); gu9188@gnu.ac.kr (H.S.); oi_sioy115@gnu.ac.kr (S.Y.L.); answns36@gnu.ac.kr (J.H.M.); sungkukkim@gnu.ac.kr (S.K.K.)
2 Korea Basic Science Institute, Daejeon 34133, Korea; jblee@kbsi.re.kr
3 Dongnam Regional Division, Korea Institute of Industrial Technology, Busan 46744, Korea; myungyoon@kitech.re.kr
* Correspondence: cwna@kitech.re.kr (C.W.N.); cjw0910@gnu.ac.kr (J.C.)

**Abstract:** Sodium ion batteries (SIBs) have drawn interest as a lithium ion battery (LIB) alternative owing to their low price and low deposits. To commercialize SIBs similar to how LIBs already have been, it is necessary to develop improved anode materials that have high stability and capacity to operate over many and long cycles. This paper reports the development of homogeneous $Sb_2S_3$ nanorods ($Sb_2S_3$ NRs) on reduced graphene oxide ($Sb_2S_3$ NRs @rGO) as anode materials for SIBs. Based on this work, $Sb_2S_3$ NRs show a discharge capacity of 564.42 mAh/g at 100 mA/g current density after 100 cycles. In developing a composite with reduced graphene oxide, $Sb_2S_3$ NRs@rGO present better cycling performance with a discharge capacity of 769.05 mAh/g at the same condition. This achievement justifies the importance of developing $Sb_2S_3$ NRs and $Sb_2S_3$ NRs@rGO for SIBs.

**Keywords:** $Sb_2S_3$ NRs@rGO; anode materials; reduced graphene oxide; sodium ion batteries



**Citation:** Hwang, H.; Seong, H.; Lee, S.Y.; Moon, J.H.; Kim, S.K.; Lee, J.B.; Myung, Y.; Na, C.W.; Choi, J. Synthesis of $Sb_2S_3$ NRs@rGO Composite as High-Performance Anode Material for Sodium-Ion Batteries. *Materials* **2021**, *14*, 7521. https://doi.org/10.3390/ma14247521

Academic Editor: Vincenzo Baglio

Received: 10 November 2021
Accepted: 2 December 2021
Published: 8 December 2021



## 1. Introduction

Until now, secondary batteries are widely used as ecofriendly energy storage. Specifically, the increasing electric car market has accelerated the development of secondary battery materials that have high capacity and stability to endure long-term electrochemical cycling [1–5]. To achieve these goals, it is essential to improve the anode's storage capacity and thus, many possible materials have been tested [6]. Although lithium ion batteries (LIBs) meet the requirements for high energy storage devices with properties of high energy density and voltage, there are limitations in using lithium because of its high price and low earthly deposits [7,8]. As a substitute to LIBs, sodium ion batteries (SIBs) have been predicted as promising batteries because of their plentiful reserves and similar energy storage mechanism to LIBs [7]. However, the large diameter of the sodium atom leads to poor diffusion efficiency of $Na^+$ and expands the anode material's volume while intercalating [9]. Therefore, it is challenging to find a proper anode material that maintains good stability with the conditions described above [10]. Among these materials, antimony sulfide ($Sb_2S_3$) is one of the strongest anode candidates that has high gravimetric energy density and theoretical capacity (946 mA/g) [11]. However, there are downsides to $Sb_2S_3$ regarding its low conductivity and volume expansion during the sodiation/desodiation process when using $Sb_2S_3$ as energy storage [12]. To solve these problems, homogeneous-width $Sb_2S_3$ nanorods ($Sb_2S_3$ NRs) and graphene oxide (GO) were used to make $Sb_2S_3$ NRs@rGO anchored on reduced graphene oxide (rGO) [13–16]. Uniform sized $Sb_2S_3$ NRs could compensate volume variation to some degrees while intercalation of Na+ than various sized nanorods [17–19]. Reduced graphene oxide (rGO) layers not only have enough interstitial spots to receive $Na^+$ but also have substantial conductivity making electron transfer easily.

Moreover, the rigid structure of rGO buffer the stress of volume expansion on $Sb_2S_3$ NRs not to make dropwise of discharge capacity of the electrode over the long term. These traits of rGO invalidate the drawback of $Sb_2S_3$ and enable the intercalation reversibly with a large amount of $Na^+$ raising capacity of the electrode [20].

Herein, this research reports the synthesis of homogeneous-width $Sb_2S_3$ NRs and $Sb_2S_3$ NRs@rGO. Through various electrochemical investigations, $Sb_2S_3$ NRs@rGO showed improved discharge capacity of 769.05 $mAhg^{-1}$ at a current density of 100 mA/g after 100 cycles. Even at a higher current density of 500 $mAg^{-1}$, excellent stability could be observed after 300 cycles, which was shown to be better than $Sb_2S_3$ NRs@rGO.

## 2. Materials and Methods

### *2.1. Synthesis of $Sb_2S_3$ NRs*

First, 10 mL of oleylamine (OAm, from Sigma-Aldrich, St. Louis, MO, USA) was heated at 150 °C for an hour under vacuum conditions to remove impurities. After heating OAm, sulfur (S, 0.0412 g, from Sigma-Aldrich, St. Louis, MO, USA) and antimony chloride ($SbCl_2$, 0.0661 g, 99%, from Sigma-Aldrich, St. Louis, MO, USA) were added to the well-dried OAm. Then the solution was heated to 230 °C over a period of 40 min with stirring and washed with 15 mL of methanol and hexane by centrifugation four times after cooling to room temperature. After that, dark gray $Sb_2S_3$ NRs powder was retrieved [21].

### *2.2. Synthesis of Graphene Oxide (GO)*

GO was prepared by the well-known Hummers method using graphite powder [20]. First, graphite (Super P, 2 g, from Timcal Ltd., Bodio, Switzerland) was added to a solution of sulfuric acid ($H_2SO_4$, 10 mL, from Samchun, Pyeongtaek, Korea), potassium persulfate ($K_2S_2O_8$, 2 g, from Sigma-Aldrich, St. Louis, MO, USA), and phosphorus pentoxide ($P_2O_5$, 2 g, from Sigma-Aldrich, St. Louis, MO, USA) at 85 °C. After stirring the mixture for 5 h, it was cooled to room temperature and 500 mL of deionized (DI) water was added for then stirred for another 12 h. The mixture was washed with DI water under vacuum filtration and dried under vacuum at room temperature. The as-prepared products were put into a cold solution of sulfuric acid ($H_2SO_4$, 100 mL, from Samchun, Pyeongtaek, Korea) while cooling in an ice bath. Potassium manganate ($KMnO_4$, 10 g, from Sigma-Aldrich, St. Louis, MO, USA) was added gradually to the resultant slurry during 1 h keeping in an ice bath. After removing an ice bath, the mixture was stirred for 24 h at room temperature. Then, 30% hydrogen peroxide ($H_2O_2$, 20 mL, from Samchun, Pyeongtaek, Korea) and DI water (500 mL) were mixed into the solution. After filtration of mixed solution, the resulting precipitate was rinsed with 10 wt % hydrochloric acid (HCl, 1 L, from Samchun, Pyeongtaek, Korea) solution in water followed by washing with DI water (1 L) to remove the acidic components.

### *2.3. Synthesis of $Sb_2S_3$ NRs@rGO*

Prepared GO was dispersed in ethanol (EtOH, 15 mL, from Samchun, Pyeongtaek, Korea) and DI water (5 mL) using ultrasonication for 1 h. $Sb_2S_3$ NRs (10 mg) were also dispersed in ethanol (EtOH, 5 mL) the same way and the two solutions were together, followed by ultrasonication for 1 h. After that, hydrazine ($N_2H_4$, 0.2 mL, from Kanto Chemical, Tokyo, Japan) was added to the solution and placed in a 250 °C oven for over 3 h and sealed with electrical tape to make reduced GO (rGO). After the supernatant liquid was removed, the retrieved product was washed with ethanol three times and dried, finally generating black/gray $Sb_2S_3$ NRs@rGO powder.

### *2.4. Structural Refinement*

A scanning electron microscope (SEM, JSM-7601F, JEOL, Tokyo, Japan) equipped with an energy dispersive spectrometer (EDS, Ultim Max, Oxford Instruments, Abingdon on Thames, UK) and transmission electron microscope (TEM, FEI RF30ST, Philips, Amsterdam, Netherlands) were used to observe the morphologies and structures of the sample. X-ray

diffraction (XRD, D8 Advance A25, Bruker, Billerica, MA, USA) was used to characterize the composition of the samples at 40 kV and 40 mA with a 0.02 s/step. Raman spectra of the samples were obtained using a Raman instrument (Renishaw InVia, Renishaw, Wotton-under-Edge, UK) with a wavelength of 633 nm. X-ray photoelectron spectroscopy (XPS) was measured using a Thermo VG scientific Sigma Probe spectrometer (Sigma probe, Thermo VG scientific, East Grinstead, UK) with a monochromatic photon energy of 1486.6 eV (Al K$\alpha$).

### *2.5. Electrochemical Investigation*

The half-coin cell (CR-2032) were assembled in a glove box filled with Ar to avoid oxygen and moisture ($O_2$ < 1 ppm, $H_2O$ < 1 ppm) contact with the Na metal used as the counter electrode. The electrode was made by mixing $Sb_2S_3$ NRs (80 wt %) with polyvinylidene fluoride (PVDF) (10 wt %) binder and super P (10 wt %). A solution of 1 M $NaPF_6$ in DEGDME is used as the electrolyte in SIBs. For comparison, $Sb_2S_3$ NRs were also made in the same way to assess the electrochemical performance. The test of galvanostatic charge-discharge was conducted in the voltage range of 0.01–3.0 V. Cyclic voltammetry (CV) measurements were carried out on a potentiostat (Zive SP1, Wonatech) at a voltage range of 0.01–3.0 V and a scanning rate of 0.05 mV/s. All electrochemical experiments above were performed at room temperature.

## 3. Results and Discussion

### *3.1. Morphology, Structure and Composition Analysis*

The shape of the $Sb_2S_3$ NRs was measured by SEM and TEM. As shown in Figure 1a,b, the $Sb_2S_3$ NRs synthesized by the hydrothermal method have smooth surfaces, showing good structural integrity. Figure 1c,d show TEM images of $Sb_2S_3$ NRs, which show a 0.36 nm lattice corresponding with the crystal plane of $Sb_2S_3$ (JCPDS No. 42-1393) [22]. These nanorods have a homogeneous-width average of 90 nm as determined via size distribution Figure 1e.

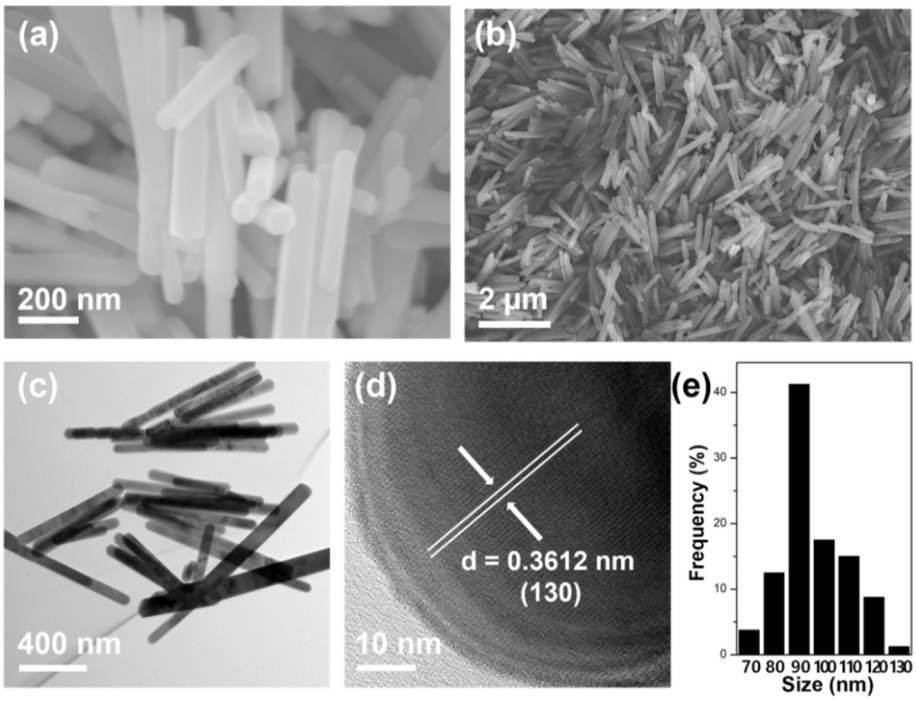


**Figure 1.** SEM Images of $Sb_2S_3$ NRs at magnification of (**a**) 80,000× and (**b**) 20,000×. TEM images of $Sb_2S_3$ NRs at magnification of (**c**) 12,000× and (**d**) 400,000×. (**e**) Size distribution of $Sb_2S_3$ NRs.

Mapping data of previous SEM images are shown in Figure 2. The SEM image of $Sb_2S_3$ NRs Figure 2a corresponds to the images of Sb Figure 2b and S Figure 2c, demonstrating homogeneity of the synthesized materials. As seen in the EDS data of Figure 2d and Table S1, 59.51 at% and 40.49 at% represent S and Sb, respectively, which proves the successful synthesis of $Sb_2S_3$ NRs (Table S1).

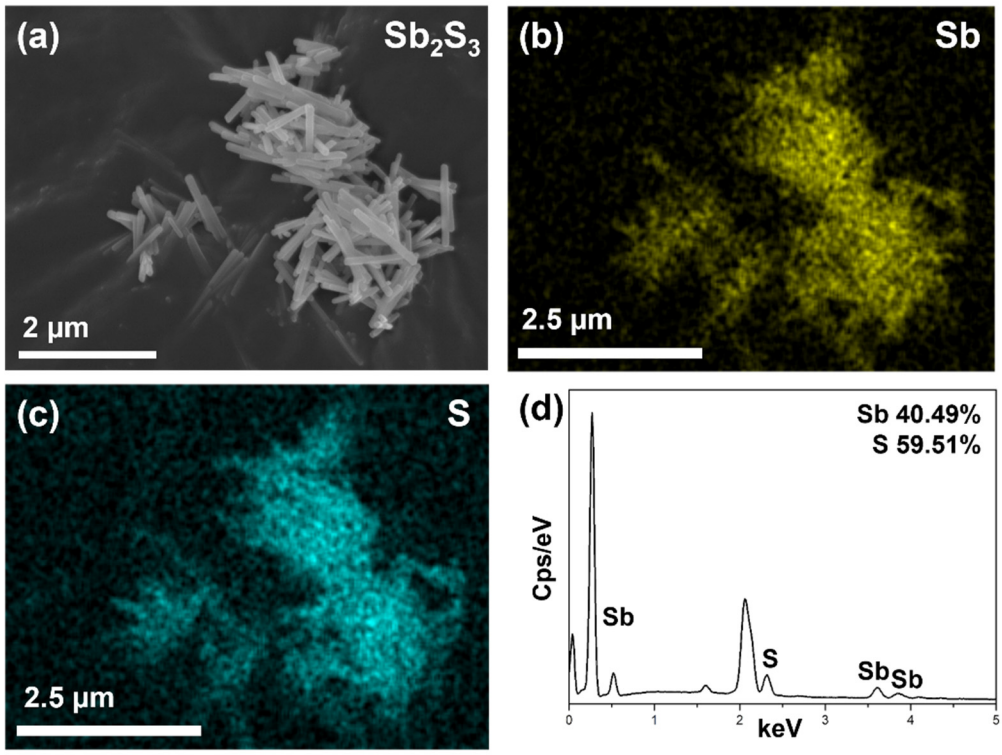


**Figure 2.** (**a**) SEM data of $Sb_2S_3$ NRs. Elemental mapping images of (**b**) Sb and (**c**) S. (**d**) EDS spectrum of Sb and S.

The modified Hummers method to synthesize the $Sb_2S_3$ NRs@rGO composite is illustrated in Figure 3. Prepared $Sb_2S_3$ NRs Figure 3a,b are anchored to rGO Figure 3c,d, where the $Sb_2S_3$ NRs particles are covered with rGO layers Figure 3e,f. Figure 4a shows the X-ray diffraction (XRD) patterns of $Sb_2S_3$ NRs, rGO, and $Sb_2S_3$ NRs@rGO. The diffraction peaks of $Sb_2S_3$ NRs correspond to the diffraction pattern of $Sb_2S_3$ (JCPDS No. 42-1393) [22], and a comparison of each peak corresponds to either $Sb_2S_3$ NRs or rGO. The electronic surroundings of C and Sb in rGO, $Sb_2S_3$, and $Sb_2S_3$ NRs @rGO were compared by X-ray photoelectron spectroscopy (XPS) in Figure 4b,c, Figure S1, Tables S2 and S3. The C 1 s orbital peaks of rGO and $Sb_2S_3$ NRs @RGO were deconvoluted into the PC1 (C-C bonding) and the PC2 (C-O bonding) bands. The C 1s orbital peaks of rGO were observed at 284.5 eV, 285.7 eV, and $Sb_2S_3$ NRs @rGO were observed at 284.5 eV, 285.8 eV. Compared to rGO, the area of PC1 decreased from 86.7% to 75.1% while that of PC2 increased from 13.3% to 24.9%. The Sb $3d_{5/2}$ and Sb $3d_{3/2}$ orbital peaks of $Sb_2S_3$ NRs were observed 528.9 eV (Sb $3d_{3/2}$) and at 538.2 eV (Sb $3d_{5/2}$) respectively. $Sb_2S_3$ NRs@rGO was deconvoluted into five bands, a PS1 at 530.2 eV and a PS2 at 531.0 eV and a PS3 at 539.5eV and a PS4 at 540.3 eV and a PO1 at 532.7 eV. The PO1 band was mostly detected from rGO. The bands of PS1 and PS3 correspond to Sb $3d_{5/2}$ and PS2 and PS4 were observed by the interaction between $Sb_2S_3$ NRs and rGO. According to the PC2 of $Sb_2S_3$ NRs@rGO in Figure 4b and PS2 and PS4 of $Sb_2S_3$ NRs@rGO in Figure 4c, The PS2 and PS4 bands were shifted to higher binding energy because the C atoms in rGO have higher electronegative than Sb atoms in $Sb_2S_3$ NRs. The result of XPS was showed that $Sb_2S_3$ NRs are incorporated on rGO [23–26]. These results prove that $Sb_2S_3$ NRs@rGO was successfully synthesized. Raman spectra of GO and $Sb_2S_3$ NRs@rGO are presented in Figure 4d. The G and D bands of $Sb_2S_3$ NRs are clearly

detected at 1586 $cm^{-1}$ and 1330 $cm^{-1}$, respectively, and a slight shift of the peaks of G and D band can be seen at 1594 $cm^{-1}$ and 1334 $cm^{-1}$, respectively, indicating the reduction of GO [27–29].

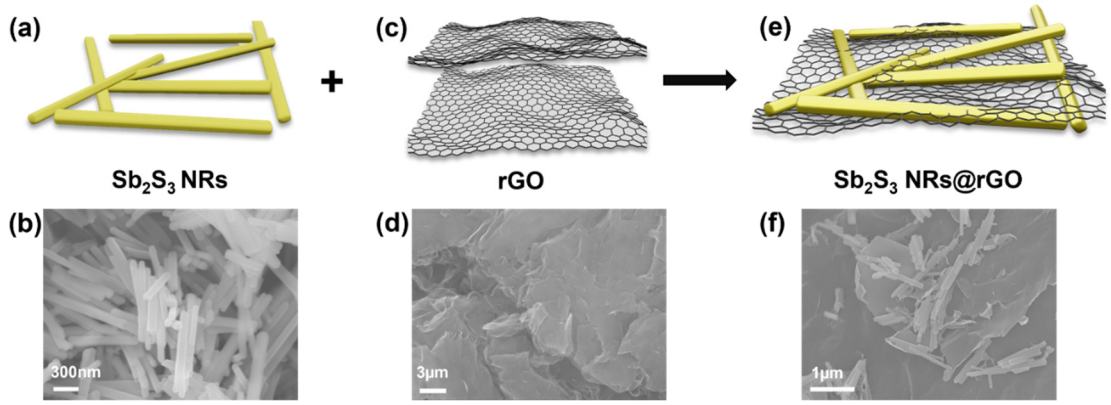


**Figure 3.** Schematic illustration of the composition with $Sb_2S_3$ NRs and reduced graphene oxide (rGO). (**a**,**b**) Illustration and SEM images of $Sb_2S_3$ NR. (**c**,**d**) Illustration and SEM images of reduced graphene oxide. (**e**,**f**) Illustration and SEM images of $Sb_2S_3$ NRs@rGO.

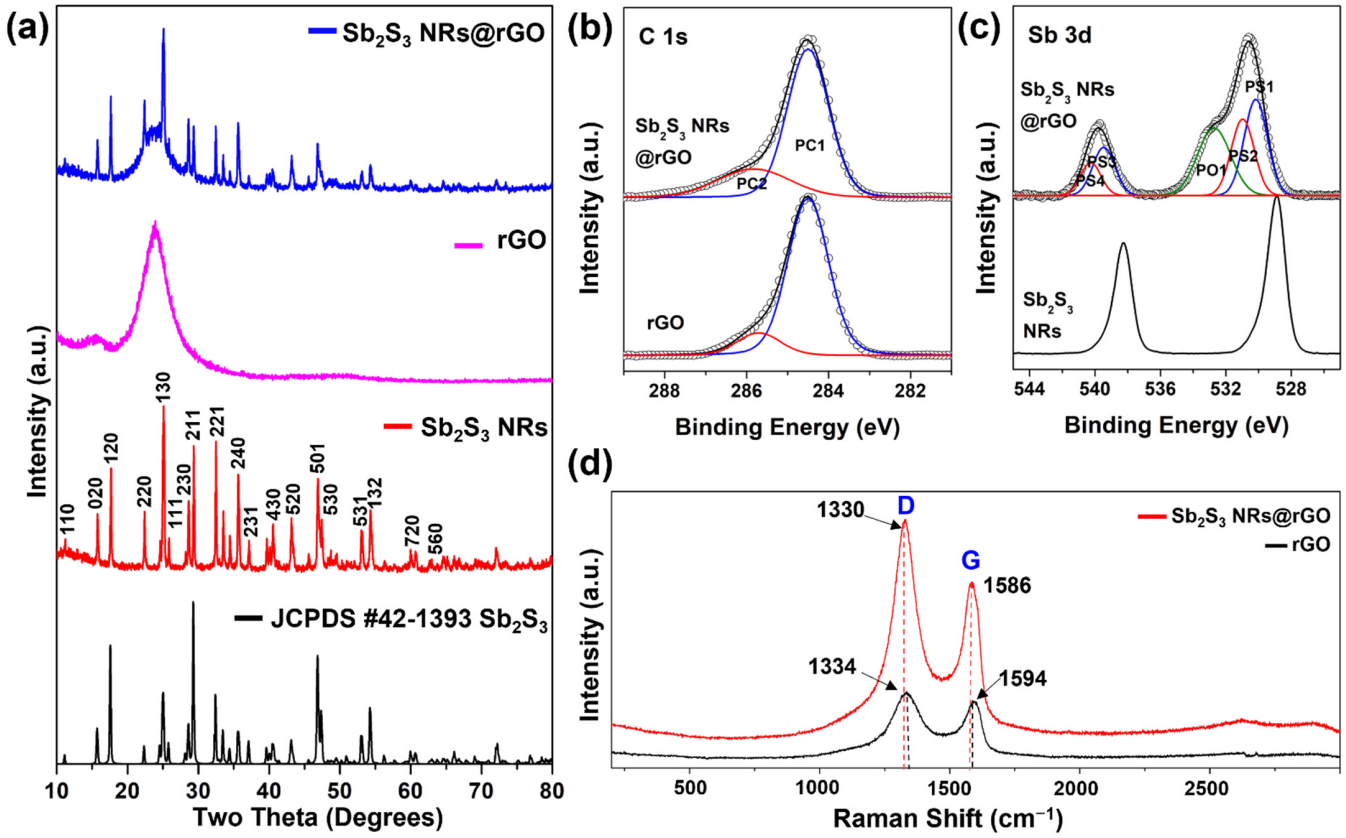


**Figure 4.** (**a**) XRD of $Sb_2S_3$ NRs, $Sb_2S_3$ NRs@rGO. (**b**) Fine-scanned C 1s of rGO and $Sb_2S_3$ NRs@rGO and (**c**) Sb 3d of $Sb_2S_3$ NRs and $Sb_2S_3$ NRs@rGO. (**d**) Raman spectrum of $Sb_2S_3$ NRs, $Sb_2S_3$ NRs@rGO.

### *3.2. Sodium Storage Behavior*

The electrochemical performances of $Sb_2S_3$ NRs and $Sb_2S_3$ NRs@rGO as anode materials in SIBs were analyzed. Figure 5a shows the CV curve of $Sb_2S_3$ NRs over the first four cycles at a scanning rate of 0.05 mV/s between 0.01 and 3.0 V (versus $Na/Na^+$). Compared with Figure 5a,b, the cathodic and anodic peaks of $Sb_2S_3$ NRs@rGO Figure 5b show remark-

able intensity. As seen in the CV of $Sb_2S_3$ NRs Figure 5a, notable cathodic peaks were not observed at 0.3 V and 1.2 V but found in $Sb_2S_3$ NRs@rGO Figure 5b, which is attributed to the conversion reaction with sulfur ($Sb_2S_3 + 6Na^+ + 6e^- \rightarrow 2Sb + 3Na_2S$) [29,30]. The anodic peaks centered at 1.1 V, 1.7 V, 2.1 V are related to the alloying reaction ($2Na_3Sb \rightarrow 2Sb + 6Na^+ + 6e^-$) and formation of $Sb_2S_3$ ($2Sb + 3Na_2S \rightarrow Sb_2S_3 + 6Na^+ + 6e^-$) in Figure 5a [29,30].

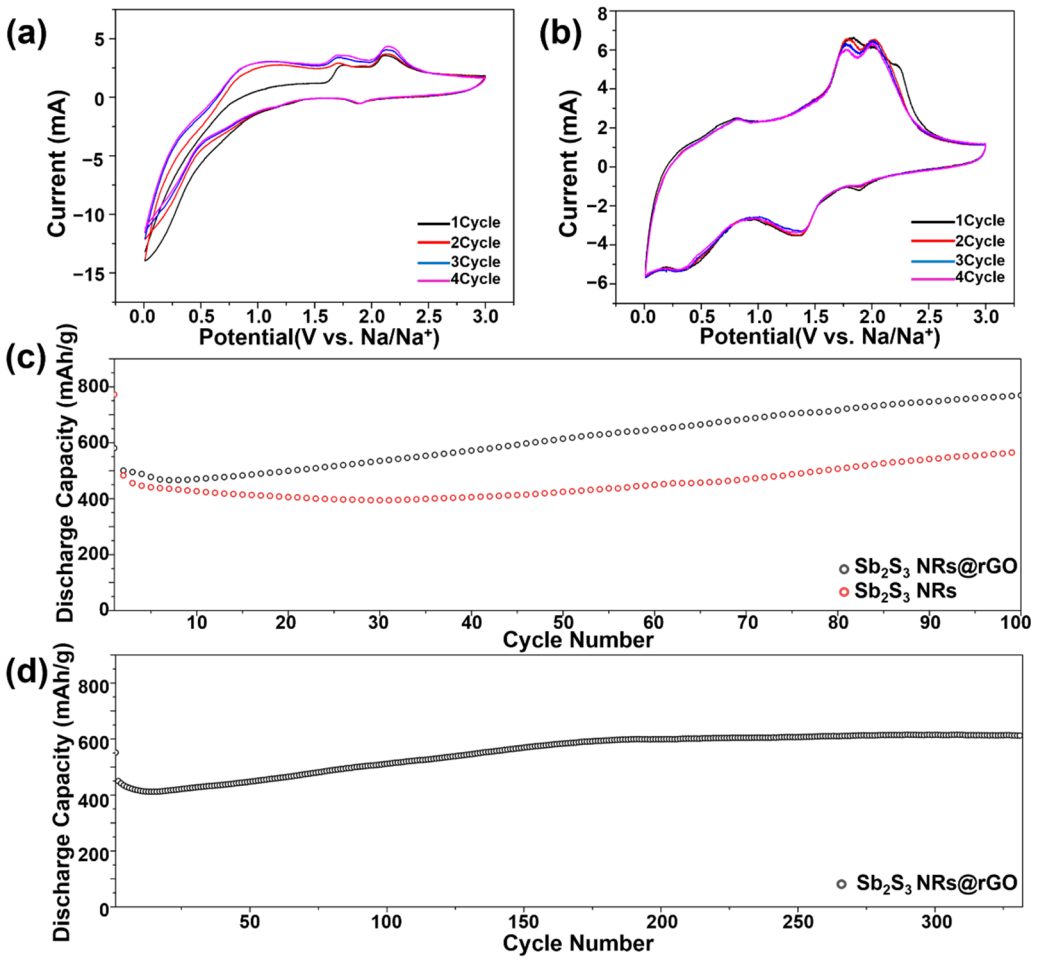


**Figure 5.** Cyclic voltammetry of (**a**) $Sb_2S_3$ NRs and (**b**) $Sb_2S_3$ NRs@rGO. Cycling performance of $Sb_2S_3$ NRs and $Sb_2S_3$ NRs@rGO at (**c**) 100D/100C and (**d**) 500D/500C.

After the composite process with rGO, there is still the same change in the cathodic process, and more remarkable peaks around 0.7 V, 1.8 V, and 2.1 V were observed in Figure 5b [29,30]. The cycling performance of $Sb_2S_3$ NRs and $Sb_2S_3$ NRs@rGO were tested at 100 $mAg^{-1}$ Figure 5c and 500 $mAg^{-1}$ Figure 5d, respectively. $Sb_2S_3$ NRs deliver a discharge capacity of 564.42 mAh/g at 100 $mAg^{-1}$ current density after 100 cycles. However, $Sb_2S_3$ NRs@rGO presents an improved cyclic performance of 769.05 $mAhg^{-1}$ at the same conditions. As shown in Figure 5d, likewise at a higher current density of 500 $mAg^{-1}$, the capacity can still attain 614.5 $mAhg^{-1}$ after 300 cycles. From Figure 5d, the discharge capacity of $Sb_2S_3$ NRs@rGO decreases from the outset and increases gradually to 300 cycles, reaching the highest discharge capacity of 614.5 $mAhg^{-1}$ at current of 500$mAg^{-1}$. This value keeps maintaining after 300 cycles. The decrease of capacity could be explained by the formation of irreversible solid electrolyte interphase (SEI) layers from the decomposition of the electrolyte [31]. Due to its electronically insulating property, irreversible capacity fading could occur. The rise of capacity could be explained by several reasons. First of all, volume expansion of $Sb_2S_3$ induces the rise of the specific capacity. As shown in Figure S2a,d, SEM images of $Sb_2S_3$ NRs and $Sb_2S_3$ NRs@rGO were presented having

homogeneous-width rod shapes. However, after several cycling tests, $Sb_2S_3$ NRs began to be expanded and defects and broken shapes were observed on its surface Figure S2b,c. As this expansion proceeds making some defects on the surface of $Sb_2S_3$ NRs, occluded reaction sites of $Sb_2S_3$ NRs also react with $Na^+$. These mounting number of reaction sites induce the increase of the capacity [31]. Secondly, the activation of materials could also attribute to this phenomenon [32–36]. Besides, the SEI layer could be constructed to be more stable during the activation process above [37]. These factors contribute to the gradual rise of the specific capacity during repeated charge and discharge which is a common activation phenomenon for chalcogenide and oxide anodes [32–36]. Even though the rise of discharge capacity looks good, this structure instability causes the variableness of electric capacity for long cycling performances. As can be seen in Figure S2d,e, $Sb_2S_3$ NRs@rGO were also expanded, though the degree of swelling was quite smaller than that of $Sb_2S_3$ NRs and could keep its rod-like shapes after several cycle performances, suggesting that reduced graphene oxide (rGO) sustains over the volume expansion of $Sb_2S_3$ NRs during sodiation and desodiation.

To examine the electrochemical kinetics of the anode materials, the electrochemical impedance spectra (EIS) of $Sb_2S_3$ NRs and $Sb_2S_3$ NRs@rGO were tested, as shown in Figure 6a [38,39]. The ohmic resistance of $Sb_2S_3$ NRs@rGO is not more than that of $Sb_2S_3$ NRs, indicating a conductivity improvement.

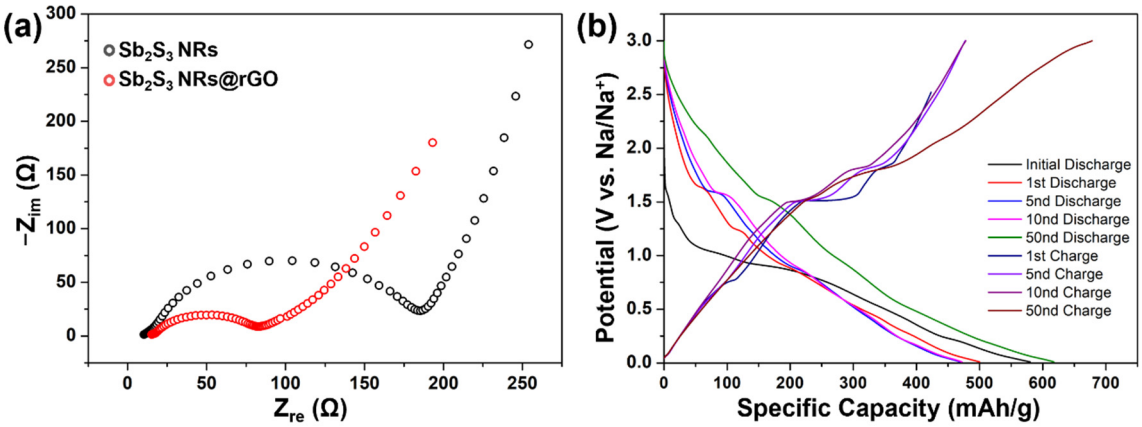


**Figure 6.** (**a**) EIS spectra of sodium ion batteries of $Sb_2S_3$ NRs and $Sb_2S_3$ NRs@rGO. (**b**) 1st, 5nd, 10nd, 50nd charge/discharge curve at a current density of 100 $mAg^{-1}$ of $Sb_2S_3$ NRs@rGO.

Figure 6b presents the galvanostatic charge/discharge profiles of $Sb_2S_3$ NRs@rGO at a current density of 100 mA/g, revealing the characteristic voltage profiles of the $Sb_2S_3$ NRs@rGO. As discussed above in Figure 5b, the conversion reaction with sulfur occurs at 0.3 V and 1.2 V, as presented by the two plateaus at similar voltages. Figure 6b alloying and formation of $Sb_2S_3$ occurs at 0.8 V, as shown by one plateau in Figure 6b. The initial discharge capacity is 580.4 mAh/g, while the second discharge delivers a capacity of 500.1 mAh/g, representing 86% coulombic efficiency. These different discharge capacities could be due to the solid electrolyte interface, which is irreversible.

## 4. Conclusions

In summary, high gravimetric energy density and theoretical capacity (946 mA/g) of $Sb_2S_3$ has been introduced as high-performance anode material for sodium ion batteries. To overcome the volume expansion of the $Sb_2S_3$, 0.9 nm $Sb_2S_3$ NRs were synthesized and then made into a composite with reduced graphene oxide. Through this work, $Sb_2S_3$ NRs@rGO showed improved discharge capacity of 769.05 mAh/g at a current density of 100 mA/g after 100 cycles and excellent stability after 300 cycles, which was shown to be better than $Sb_2S_3$ NRs. This paper has developed a novel synthetic process for $Sb_2S_3$ NRs and $Sb_2S_3$ NRs@rGO and presents an avenue in determining more suitable anode materials for SIBs.

**Supplementary Materials:** The following are available online at https://www.mdpi.com/article/10.3390/ma14247521/s1, Figure S1: XPS survey spectrum of $Sb_2S_3$ NRs and $Sb_2S_3$ NRs@rGO, Figure S2: SEM images of $Sb_2S_3$ NRs before cyclic test (a) and after several cyclic test (b), Table S1: EDS elemental qualification results, Table S2: Fine-scanned data of C 1s in rGO and $Sb_2S_3$ NRs@rGO, Table S3: Fine-scanned data of Sb 3d and O 1s in $Sb_2S_3$ NRs and $Sb_2S_3$ NRs@rGO.

**Author Contributions:** Conceptualization and investigation: H.H. and S.Y.L.; software: H.S. and J.H.M.; data curation: J.B.L.; formal analysis: H.H. and Y.M.; writing—review and editing: S.K.K. and C.W.N.; supervision: J.C.; project administration: J.C. All authors have read and agreed to the published version of the manuscript.

**Funding:** This research was supported by the International Research & Development Program of the National Research Foundation of Korea (NRF) grant funded by the Korea government(MSIT), Regional Innovation Strategy (RIS), Ministry of Science, ICT, and Future Planning (MSIP) of Korea (NRF-2019R1F1A1059131, NRF-2020R1F1A1072441, NRF-2021R1C1C1011436).

**Institutional Review Board Statement:** Not applicable.

**Informed Consent Statement:** Not applicable.

**Data Availability Statement:** The data presented in this study are contained within the article.

**Conflicts of Interest:** The authors declare no conflict of interest.

## References

1. Goodenough, J.B.; Kim, Y. Challenges for Rechargeable Li Batteries. *Chem. Mater.* **2019**, *22*, 587–603. [CrossRef]
2. Xin, F.; Whittingham, M.S. Challenges and Development of Tin-Based Anode with High Volumetric Capacity for Li-Ion Batteries. *Electrochem. Energy Rev.* **2020**, *3*, 643–655. [CrossRef]
3. Wen, J.; Pei, Y.; Liu, L.; Su, D.; Yang, M.; Wang, Q.; Zhang, W.; Dai, J.; Feng, Y.; Wu, T.; et al. Fully encapsulated Sb2Se3/Sb/C nanofibers: Towards high-rate, ultralong-lifespan lithium-ion batteries. *J. Alloys Compd.* **2021**, *874*, 159961. [CrossRef]
4. Hwang, J.Y.; Myung, S.T.; Sun, Y.K. Sodium-ion batteries: Present and future. *Chem. Soc. Rev.* **2017**, *46*, 3529–3614. [CrossRef]
5. Dashairya, L.; Das, D.; Saha, P. Elucidating the role of graphene and porous carbon coating on nanostructured Sb2S3 for superior lithium and sodium storage. *J. Alloys Compd.* **2021**, *883*, 160906. [CrossRef]
6. Zhao, Y.; Manthiram, A. Amorphous Sb2S3 embedded in graphite: A high-rate, long-life anode material for sodium-ion batteries. *Chem. Commun.* **2015**, *51*, 13205–13208. [CrossRef] [PubMed]
7. Yao, S.; Cui, J.; Lu, Z.; Xu, Z.-L.; Qin, L.; Huang, J.; Sadighi, Z.; Ciucci, F.; Kim, J.-K. Unveiling the Unique Phase Transformation Behavior and Sodiation Kinetics of 1D van der Waals Sb2S3Anodes for Sodium Ion Batteries. *Adv. Energy Mater.* **2017**, *7*, 1602149. [CrossRef]
8. Li, J.; Yan, D.; Zhang, X.; Hou, S.; Li, D.; Lu, T.; Yao, Y.; Pan, L. In situ growth of Sb2S3 on multiwalled carbon nanotubes as high-performance anode materials for sodium-ion batteries. *Electrochim. Acta* **2017**, *228*, 436–446. [CrossRef]
9. Tarascon, J.M.; Armand, M. Issues and challenges facing rechargeable lithium batteries. *Nature* **2001**, *414*, 359–367. [CrossRef] [PubMed]
10. Zhu, Y.; Nie, P.; Shen, L.; Dong, S.; Sheng, Q.; Li, H.; Luo, H.; Zhang, X. High rate capability and superior cycle stability of a flower-like Sb2S3 anode for high-capacity sodium ion batteries. *Nanoscale* **2015**, *7*, 3309–3315. [CrossRef] [PubMed]
11. Hou, H.S.; Jing, M.J.; Huang, Z.D.; Yang, Y.C.; Zhang, Y.; Chen, J.; Wu, Z.B.; Ji, X.B. One-Dimensional Rod-Like Sb2S3-Based Anode for High-Performance Sodium-Ion Batteries. *ACS Appl. Mater. Interfaces* **2015**, *7*, 19362–19369. [CrossRef]
12. Hameed, A.S.; Reddy, M.V.; Chen, J.L.T.; Chowdari, B.V.R.; Vittal, J.J. RGO/Stibnite Nanocomposite as a Dual Anode for Lithium and Sodium Ion Batteries. *ACS Sustain. Chem. Eng.* **2016**, *4*, 2479–2486. [CrossRef]
13. Chen, B.; Lu, H.; Zhou, J.; Ye, C.; Shi, C.; Zhao, N.; Qiao, S.-Z. Porous MoS2/Carbon Spheres Anchored on 3D Interconnected Multiwall Carbon Nanotube Networks for Ultrafast Na Storage. *Adv. Energy Mater.* **2018**, *8*, 1702909. [CrossRef]
14. Hong, Y.R.; Mhin, S.; Kwon, J.; Han, W.S.; Song, T.; Han, H. Synthesis of transition metal sulfide and reduced graphene oxide hybrids as efficient electrocatalysts for oxygen evolution reactions. *R. Soc. Open Sci.* **2018**, *5*, 180927. [CrossRef]
15. Li, G.; Luo, D.; Wang, X.; Seo, M.H.; Hemmati, S.; Yu, A.; Chen, Z. Enhanced Reversible Sodium-Ion Intercalation by Synergistic Coupling of Few-Layered MoS2and S-Doped Graphene. *Adv. Funct. Mater.* **2017**, *27*, 1702562. [CrossRef]
16. Wang, B.; Ruan, T.; Chen, Y.; Jin, F.; Peng, L.; Zhou, Y.; Wang, D.; Dou, S. Graphene-based composites for electrochemical energy storage. *Energy Storage Mater.* **2020**, *24*, 22–51. [CrossRef]
17. Deng, P.; Yang, J.; He, W.; Li, S.; Zhou, W.; Tang, D.; Qu, B. Tin-Assisted Sb2S3Nanoparticles Uniformly Grafted on Graphene Effectively Improves Sodium-Ion Storage Performance. *ChemElectroChem* **2018**, *5*, 811–816. [CrossRef]
18. Jiang, Y.; Wei, M.; Feng, J.; Ma, Y.; Xiong, S. Enhancing the cycling stability of Na-ion batteries by bonding SnS2ultrafine nanocrystals on amino-functionalized graphene hybrid nanosheets. *Energy Environ. Sci.* **2016**, *9*, 1430–1438. [CrossRef]

19. Youn, D.H.; Stauffer, S.K.; Xiao, P.; Park, H.; Nam, Y.; Dolocan, A.; Henkelman, G.; Heller, A.; Mullins, C.B. Simple Synthesis of Nanocrystalline Tin Sulfide/N-Doped Reduced Graphene Oxide Composites as Lithium Ion Battery Anodes. *ACS Nano* **2016**, *10*, 10778–10788. [CrossRef] [PubMed]
20. Choi, B.G.; Park, H.; Park, T.J.; Yang, M.H.; Kim, J.S.; Jang, S.Y.; Heo, N.S.; Lee, S.Y.; Kong, J.; Hong, W.H. Solution chemistry of self-assembled graphene nanohybrids for high-performance flexible biosensors. *ACS Nano* **2010**, *4*, 2910–2918. [CrossRef]
21. Park, K.H.; Choi, J.; Kim, H.J.; Lee, J.B.; Son, S.U. Synthesis of antimony sulfide nanotubes with ultrathin walls via gradual aspect ratio control of nanoribbons. *Chem. Mater.* **2007**, *19*, 3861–3863. [CrossRef]
22. Xiong, X.; Wang, G.; Lin, Y.; Wang, Y.; Ou, X.; Zheng, F.; Yang, C.; Wang, J.H.; Liu, M. Enhancing Sodium Ion Battery Performance by Strongly Binding Nanostructured Sb2S3 on Sulfur-Doped Graphene Sheets. *ACS Nano* **2016**, *10*, 10953–10959. [CrossRef]
23. Lu, Y.; Zhang, N.; Jiang, S.; Zhang, Y.; Zhou, M.; Tao, Z.; Archer, L.A.; Chen, J. High-Capacity and Ultrafast Na-Ion Storage of a Self-Supported 3D Porous Antimony Persulfide-Graphene Foam Architecture. *Nano Lett.* **2017**, *17*, 3668–3674. [CrossRef] [PubMed]
24. Stankovich, S.; Dikin, D.A.; Piner, R.D.; Kohlhaas, K.A.; Kleinhammes, A.; Jia, Y.; Wu, Y.; Nguyen, S.T.; Ruoff, R.S. Synthesis of graphene-based nanosheets via chemical reduction of exfoliated graphite oxide. *Carbon* **2007**, *45*, 1558–1565. [CrossRef]
25. Stankovich, S.; Piner, R.D.; Chen, X.; Wu, N.; Nguyen, S.T.; Ruoff, R.S. Stable aqueous dispersions of graphitic nanoplatelets via the reduction of exfoliated graphite oxide in the presence of poly(sodium 4-styrenesulfonate). *J. Mater. Chem.* **2006**, *16*, 155–158. [CrossRef]
26. Choi, J.; Myung, Y.; Kim, S.-K. Flexible sodium-ion battery anodes using indium sulfide-based nanohybrid paper electrodes. *Appl. Surf. Sci.* **2019**, *467–468*, 1040–1045. [CrossRef]
27. Peng, S.; Han, X.; Li, L.; Zhu, Z.; Cheng, F.; Srinivansan, M.; Adams, S.; Ramakrishna, S. Unique Cobalt Sulfide/Reduced Graphene Oxide Composite as an Anode for Sodium-Ion Batteries with Superior Rate Capability and Long Cycling Stability. *Small* **2016**, *12*, 1359–1368. [CrossRef] [PubMed]
28. Baggetto, L.; Ganesh, P.; Sun, C.-N.; Meisner, R.A.; Zawodzinski, T.A.; Veith, G.M. Intrinsic thermodynamic and kinetic properties of Sb electrodes for Li-ion and Na-ion batteries: Experiment and theory. *J. Mater. Chem. A* **2013**, *1*, 7985–7994. [CrossRef]
29. Wang, S.; Yuan, S.; Yin, Y.-B.; Zhu, Y.-H.; Zhang, X.-B.; Yan, J.-M. Green and Facile Fabrication of MWNTs@Sb2S3@PPy Coaxial Nanocables for High-Performance Na-Ion Batteries. *Part. Part. Syst. Charact.* **2016**, *33*, 493–499. [CrossRef]
30. Pan, Z.-Z.; Yan, Y.; Cui, N.; Xie, J.-C.; Zhang, Y.-B.; Mu, W.-S.; Hao, C. Ionic Liquid-Assisted Preparation of Sb2S3/Reduced Graphene Oxide Nanocomposite for Sodium-Ion Batteries. *Adv. Mater. Interfaces* **2018**, *5*, 1701481. [CrossRef]
31. Fan, A.; Hou, T.; Sun, X.; Xie, D.; Li, X.; Zhang, N.; Guo, J.; Jin, S.; Zhou, Y.; Cai, S.; et al. One-Pot Hydrothermal Synthesis of ZnS Nanospheres Anchored on 3D Conductive MWCNTs Networks as High-Rate and Cold-Resistant Anode Materials for Sodium-Ion Batteries. *ChemElectroChem* **2020**, *7*, 1904–1913. [CrossRef]
32. Dong, Y.; Hu, M.; Zhang, Z.; Zapien, J.A.; Wang, X.; Lee, J.M. Hierarchical self-assembled Bi2S3 hollow nanotubes coated with sulfur-doped amorphous carbon as advanced anode materials for lithium ion batteries. *Nanoscale* **2018**, *10*, 13343–13350. [CrossRef]
33. Guo, B.; Fang, X.; Li, B.; Shi, Y.; Ouyang, C.; Hu, Y.-S.; Wang, Z.; Stucky, G.D.; Chen, L. Synthesis and Lithium Storage Mechanism of Ultrafine MoO2 Nanorods. *Chem. Mater.* **2012**, *24*, 457–463. [CrossRef]
34. Liang, H.; Ni, J.; Li, L. Bio-inspired engineering of Bi2S3-PPy yolk-shell composite for highly durable lithium and sodium storage. *Nano Energy* **2017**, *33*, 213–220. [CrossRef]
35. Ni, J.; Zhao, Y.; Li, L.; Mai, L. Ultrathin MoO2 nanosheets for superior lithium storage. *Nano Energy* **2015**, *11*, 129–135. [CrossRef]
36. Shi, Y.; Guo, B.; Corr, S.A.; Shi, Q.; Hu, Y.S.; Heier, K.R.; Chen, L.; Seshadri, R.; Stucky, G.D. Ordered mesoporous metallic MoO2 materials with highly reversible lithium storage capacity. *Nano Lett.* **2009**, *9*, 4215–4220. [CrossRef]
37. Hu, Y.Y.; Liu, Z.; Nam, K.W.; Borkiewicz, O.J.; Cheng, J.; Hua, X.; Dunstan, M.T.; Yu, X.; Wiaderek, K.M.; Du, L.S.; et al. Origin of additional capacities in metal oxide lithium-ion battery electrodes. *Nat. Mater.* **2013**, *12*, 1130–1136. [CrossRef]
38. Wen, S.; Zhao, J.; Zhao, Y.; Xu, T.; Xu, J. Reduced graphene oxide (RGO) decorated Sb2S3 nanorods as anode material for sodium-ion batteries. *Chem. Phys. Lett.* **2019**, *716*, 171–176. [CrossRef]
39. Bag, S.; Roy, A.; Mitra, S. Sulfur, nitrogen dual doped reduced graphene oxide supported two-dimensional Sb2S3 nanostructures for the anode material of sodium-ion battery. *Chem. Sel.* **2019**, *4*, 6679–6686.